

Solid-State Synthesis and Optical Studies of Water-Stable Pb^{2+} -Doped Mn^{2+} Complexes

Qiankai Ba, Abhishek Meena, and Atanu Jana*



Cite This: <https://doi.org/10.1021/acs.inorgchem.3c02840>



Read Online

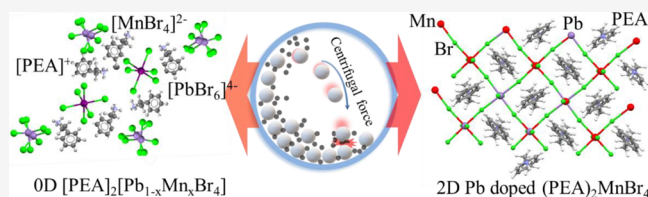
ACCESS |

Metrics & More

Article Recommendations

Supporting Information

ABSTRACT: The limited Mn^{2+} doping that occurs in lead halide perovskites has been widely described, while the Pb^{2+} doping that occurs in Mn^{2+} halide perovskites has not been studied well. Generally, a large amount of doping of Mn^{2+} in lead halide perovskite degrades the perovskite structure; eventually, high orange luminescence of Mn^{2+} dopant has not been achieved. In our present study, we followed a reverse strategy, i.e., Pb^{2+} doping in Mn^{2+} halide perovskites, to increase the amount of Mn^{2+} in halide perovskites through the high-energy ball milling method. This strategy yields bright-fluorescence orange light-emitting Mn^{2+} -doped perovskite with a Mn/Pb ratio of 95%, which is the highest among Mn^{2+} -doped perovskites. Zero-dimensional (0D) Mn^{2+} perovskites and two-dimensional (2D) Pb^{2+} -doped Mn^{2+} -based perovskites were successfully synthesized and characterized. During the mechanochemical engineering, Pb^{2+} ions partially occupy the site of Mn^{2+} ions and act as a luminescence activator. Mn^{2+} -based 2D perovskites with the proper amounts of Pb^{2+} ions as dopant ions and phenylethylammonium (PEA^+) as dielectric organic cations show enhanced stability in water. The dual-emissive properties of these 2D- Pb^{2+} -doped Mn^{2+} -based perovskites were also investigated by using single-particle imaging fluorescence. We believe that these findings will pave the way for designing eco-friendly dimension and bandgap tunable layered perovskites.



INTRODUCTION

Doping of Mn^{2+} ions in wide-band-gap semiconductors has been proven to be a lucrative idea started by Bhargava and co-workers back in 1994.¹ In 2016, the Klimov group extended it to lead halide perovskite nanocrystals, achieving highly efficient Mn d–d emission.² Since then, numerous reports of Mn^{2+} doping in perovskites have been documented. The unique characteristics of Mn^{2+} doping are easily identifiable by its orange emission centered within 580–600 nm and its long excited-state decay lifetime due to ${}^4\text{T}_{1g}$ to ${}^6\text{A}_{1g}$ transition of centrosymmetric $[\text{MnX}_6]^{4-}$.^{3,4} These doped nanocrystals have gained tremendous interest in several applications, such as solar cells,^{5–7} water splitting,⁸ and light-emitting devices.^{9,10}

Nowadays, development of low-toxicity Pb-free perovskites has mainly focused on the substituent of Pb in 3D or 2D structures with transition metal and rare earth metal cations.^{3,11–18} Replacing toxic lead in lead-free perovskite materials with lead-free elements like manganese (Mn),^{16,19} copper (Cu),^{15,18} antimony (Sb),¹⁷ and bismuth (Bi)²⁰ is indeed a critical step in addressing the environmental and health concerns associated with lead toxicity, especially in emerging technologies like perovskite solar cells²¹ and light-emitting diodes (LEDs).²² However, it has raised stability concerns since the B-site cations in low dopant ion concentrations are easily oxidized, which induces the stain defect leading to the decomposition of perovskite structure.²³ Notably, the widely used synthetic approaches for Mn^{2+} -doped perovskites are bottom-up strategies, which produce perov-

skites via nucleation/growth of precursor ions in solution.¹³ In situ or postsynthetic Mn^{2+} doping in host nanocrystals^{24–28} and solvothermal synthesis¹³ were widely reported to obtain Mn^{2+} -doped perovskites. Recently, an acid solution-assisted method at room temperature was also explored to synthesize layered Mn^{2+} -doped L_2PbBr_4 .²⁹ Despite that these strategies for Mn^{2+} doping have been adopted, it is surprising that the reverse doping strategy, i.e., Pb^{2+} doping in Mn halide perovskites, has been completely overlooked. This strategy can reduce the toxicity of perovskites and boost the efficient exciton energy transfer, leading to intense orange emission of a large number of Mn^{2+} ions. Furthermore, although solution-processed doping of Mn^{2+} ions into lead halide perovskites is extensively studied, the chemistry of Mn doping in 2D-layered perovskites has been rarely explored.^{27,28} Despite several efforts for Mn doping in perovskite, only a small fraction of Mn^{2+} was incorporated into layered hybrid perovskite crystals. This is attributed to the large formation energy of B-site-doped ABX_3 or A_2BX_4 perovskite³⁰ and the large difference in atomic radii of Pb^{2+} and Mn^{2+} , which causes

Received: August 15, 2023

Revised: October 17, 2023

Accepted: October 17, 2023

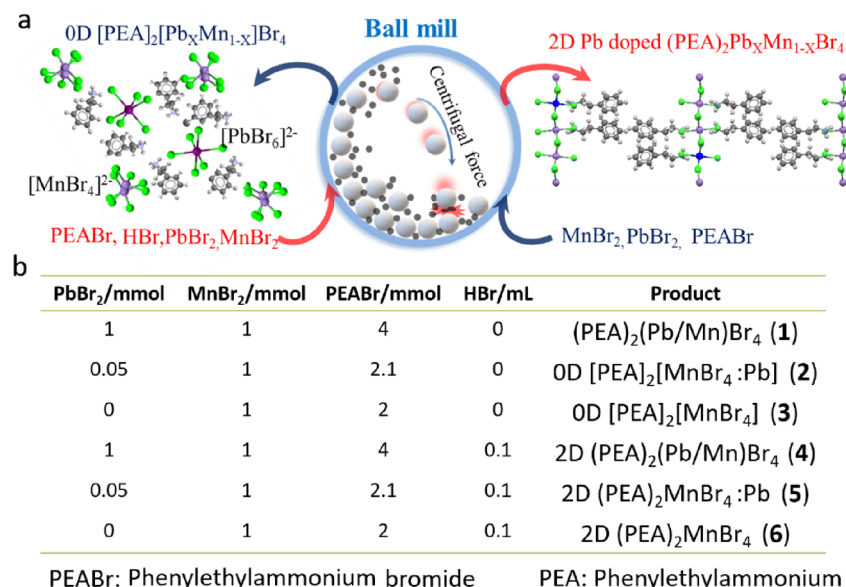


Figure 1. (a) Schematic representation of ball milling synthesis of 2D and 0D perovskites. (b) List of all synthesized compounds **1–6** with different precursors.

lattice strain leading to the destruction of perovskite geometry.³⁰ Another critical factor for determining the emission energy, which depends on the coordination environment of Mn²⁺, was not investigated extensively because of the concentration limitation in Mn²⁺ ion doping.

Here, we demonstrate the PEA⁺-assisted formation of water-stable 0D-Mn²⁺ perovskites and 2D-Pb²⁺-doped Mn²⁺-based perovskites (Figure 1). PEA⁺ is an ideal component for creating water-stable perovskite because of its excellent hydrophobicity.^{29,31} The ball milling in Figure 1a shows the motion of the balls and precursors. The detailed structural information and raw materials are given in Figure 1b. The precursors in ball mill are subjected to high-energy collision from balls; thus, the bond-reforming and phase transformation occur, forming Mn-based perovskite.

The proper ratio of Mn/Pb in 2D perovskites (**4** and **5**) greatly enhances the water stability of these materials. Generally, Mn–Mn symmetry-directed spin-exchange interactions cause photoluminescence (PL) quenching in pure Mn complexes, whereas distance-directed Mn–Mn dipole–dipole interactions increase the PL intensity.³² As the Mn–Mn distance in our as-synthesized materials is increased due to lattice swelling caused by the substitution of Mn²⁺ by Pb²⁺,³³ the distance-directed Mn–Mn dipole–dipole interactions is dominant over the symmetry-directed spin-exchange interactions, leading to an overall increase in PL intensity. The synthesized 2D-Pb²⁺-doped Mn²⁺-based perovskites show excellent stability in water. We have also carried out single-particle imaging fluorescence to explore the dual-emissive nature of these 2D-Pb²⁺-doped Mn²⁺-based perovskites.

EXPERIMENTAL SECTION

Materials. We utilized all commercially available reagents as received unless otherwise specified. PbBr₂ ($\geq 98\%$), MnBr₂ (98%), and HBr (48% in water) were purchased from Sigma-Aldrich. Phenylethylamine (PEA, > 99%) was purchased from Tokyo Chemical Industry (TCI).

General Synthesis Process for Pb²⁺-Doped Mn²⁺-Perovskite Compounds. Initially, a ball-mill container was loaded with 20 g of zirconium oxide balls and MBr₂ (M = Pb or Mn). After sealing the

vessel, milling commenced for 5 min. Subsequently, the mixture was milled for an additional 10 min in the presence of phenylethylammonium bromide (PEABr) under the same conditions. The resulting product was then dried at 50 °C overnight, yielding a yellowish-white powder.

(PEA)₂(Pb/Mn)Br₄ (**1**). PbBr₂ (0.38 g, 1 mmol), MnBr₂ (0.21 g, 1 mmol), and PEABr (0.8 g, 4 mmol).

OD [PEA]₂[MnBr₄:Pb] (**2**). PbBr₂ (0.025 g, 0.067 mmol), MnBr₂ (0.21 g, 1 mmol), and PEABr (0.42 g, 2.1 mmol).

OD [PEA]₂[MnBr₄] (**3**). MnBr₂ (0.21 g, 1 mmol) and PEABr (0.4 g, 2 mmol).

2D (PEA)₂(Mn/Pb)Br₄ (**4**). PbBr₂ (0.38 g, 1 mmol), MnBr₂ (0.21 g, 1 mmol), 0.1 mL of HBr acid solution, and PEABr (0.8 g, 4 mmol).

2D (PEA)₂MnBr₄:Pb (**5**). Under the general synthesis procedure, PbBr₂ (0.025 g, 0.067 mmol), MnBr₂ (0.21 g, 1 mmol), 0.1 mL of HBr acid solution, and PEABr (0.42 g, 2.1 mmol).

2D (PEA)₂MnBr₄ (**6**). MnBr₂ (0.21 g, 1 mmol), 0.1 mL of HBr acid solution, and PEABr (0.4 g, 2 mmol).

Physical Measurements. Powder X-ray diffraction (PXRD) analyses were conducted by using a Rigaku D Max 2500 V PC diffractometer with a Cu-rotating anode X-ray source. The PXRD data was collected employing a K-alpha model from Thermo Fisher. The measurements covered a Bragg's diffraction angle (2θ) range of 5–50° at a scan rate of 2° per minute. Scanning electron microscopy (SEM) images were captured with a Hitachi High-Technologies SU8220 Cold FE-SEM, operating at an acceleration voltage of 10 kV. Elemental characterization of all samples was performed by using energy-dispersive X-ray spectroscopy (EDX). X-ray photoelectron spectroscopy (XPS) was conducted using a K-Alpha instrument from Thermo Fisher to analyze the chemical compositions. The optical diffuse reflectance spectra of the solid samples were obtained by using an Agilent Cary 5000 UV–Vis–NIR spectrophotometer equipped with an integrated sphere in the diffuse-reflectance mode. Subsequently, these spectra were transformed into the Kubelka–Munk function, $F(R)$. For a comprehensive understanding of the PL characteristics in perovskite materials with varying dimensionalities and compositions, we employ single-particle fluorescence microscopy. This is coupled with PL emission spectral analysis to study PL properties at the individual particle level using a 405 nm laser. PL microscopy images and single-particle PL spectra were acquired by using an LSM 780 NLO microscope from Carl Zeiss. The measurements were conducted under a single channel spanning 405 to 680 nm, with the powder samples dispersed on glass slides, and the 405 nm laser was used throughout the study. We obtained room-temperature PL

spectra for all solid compounds in their solid state by using a Varian Cary Eclipse fluorometer. The photoluminescence quantum yield (PLQY) of the solid samples was determined experimentally with a Jasco International FP-8500 ST spectrophotofluorometer, employing an integrating sphere. PLQY was evaluated by integrating the sphere, and the following equations were used: $\text{PLQY} [\%] = S_2 / (S_0 - S_1) \times 100$; S_0 = area from incident light, S_1 = area scattered from the sample, S_2 = area emitted from sample, S_0 was measured with nothing in the sample holder.

RESULTS AND DISCUSSION

The detailed synthetic procedures of all the materials shown in Figure 1b are described in the Supporting Information. In the synthesis of 2D Pb^{2+} -doped and undoped Mn^{2+} -based perovskites, the addition of 0.1 mL of HBr plays a multifaceted role. First, HBr acts as an acid catalyst, accelerating the reaction kinetics during the milling process. This catalytic effect promotes the efficient formation of intermediates and aids in achieving the desired perovskite crystal structure. Second, HBr contributes to the control and homogeneity of the reaction by influencing the rate of milling and ensuring uniform mixing of the reactants. Additionally, it plays a role in stabilizing reaction intermediates, preventing their decomposition, and facilitating the formation of the target perovskite phase. The addition of 0.1 mL of HBr is crucial for enhancing the synthesis efficiency and the quality of the resulting 2D perovskite materials. To verify the structures of 1–6, X-ray diffraction (XRD) measurements are carried out (Figure 1). The typical 2D-layered structures 4–6 are observed in Figure 2a.^{34,35} These structures are identified with their optical

shift to a higher angle as the Mn^{2+} ion concentration increases (Figure S2).² However, multiphases are observed in the XRD patterns of 4 and 5, corresponding to the Pb^{2+} -rich and -poor phases, respectively, which exhibit main peaks at 5.52 and 5.28°, respectively.^{27,38} The Pb^{2+} -poor phase presents peak patterns similar to the XRD pattern of 6, indicating the 2D-layered structure formation. Thus, sufficient anions induced the formation of the 2D structure under high-energy ball milling. In the XRD patterns of 2 and 3, the peak at 11.08° disappears, ruling out the possibility of forming a layered structure.³⁹ However, 1 exhibits the layered structure pattern along with the adsorption spectra of coexisting 0D and 2D structures. We predict that the Pb^{2+} -hybrid halide forms along with the 0D structure formation. As a result, the Mn^{2+} characteristic emission PL quantum yield (QY) for 1 reaches the highest among the six compounds reported here.

The optical properties of all of the compounds are studied by solid-state diffuse reflectance and PL (Figure 2c,d). 3 exhibits multipeaks centered at 363, 376, 392, 438, 455, and 472 nm, which are associated with the transitions of $[\text{MnBr}_4]^{2-}$ (T_d) tetrahedral from ground state $^6\text{A}_1$ (S) to excited states $^4\text{T}_2(^4\text{D})$, $^4\text{E}(^4\text{D})$, $^4\text{E}(^4\text{G})$, $^4\text{A}_1(^4\text{G})$, $^4\text{T}_2(^4\text{G})$, and $^4\text{T}_1(^4\text{G})$, respectively.^{4,40} In Figure 2c, a sharp peak appears at 401 nm and a weak absorption peak at 391 nm after Pb^{2+} doping for 2, which are associated with the octahedral crystal-field transitions.^{4,41} $[\text{PbBr}_6]^{4-}$ octahedron moieties and Pb^{2+} atoms are partially substituted by Mn^{2+} ions. We determine that 2 and 3 are in the 0D phase. When the Pb/Mn ratio increases to 1, 1 exhibits one sharp peak centered at 409 nm and a broad band tail extends to 600 nm, which are attributed to the absorption of $[\text{PbBr}_6]^{4-}$ and $[\text{MnBr}_4]^{2-}$, respectively.⁴² This strengthens the evidence of a mixture of phases in 1, corroborated with the XRD pattern. Previously, there are several reports for appearance of two PL peaks of Mn-doped 2D PEA_2PbX_4 perovskites in the blue and red regions.^{35,43,44} The blue emission is from the 2D PEA_2PbX_4 lattice, and the red emission corresponds to the $[\text{MnBr}_6]^{4-}$ moiety. It is well known that $[\text{MnBr}_6]^{4-}$ and $[\text{MnBr}_4]^{2-}$ moieties are responsible for orange emission and green emission, respectively.⁴ Mir et al. have previously demonstrated the substitution of Mn^{2+} ions for octahedrally coordinated Pb^{2+} ions in the lattice of halide perovskite, supported by an electron paramagnetic resonance (EPR) study.⁴³ As for 6, because of the forbidden transition of Mn^{2+} in the 2D perovskite structure, nearly no absorption peak is observed in the UV-vis spectra. 4 and 5 show the characteristic peaks of a 2D-layered Mn/Pb hybrid structure.²⁹ More evidence is provided to confirm the structural information via PL spectra in Figure 2d. Generally, the $\text{Mn}(\text{II})$ emission in the O_h geometry is known to be in the red region, which is due to the weaker octahedral ligand field, as compared to the T_d geometry.⁴⁶ 1, 2, 4, and 5 show the featured energy transfer from the Pb^{2+} activator to the Mn^{2+} emitter in the presence of the octahedral crystal field. 1 and 2 show main Mn^{2+} characteristic emission peaks ($^6\text{A}_{1g}$ – $^4\text{T}_{1g}$) and weak Pb^{2+} emission peaks because of better efficient energy transfer under the 0D structure.⁴⁷

To identify the composition and understand the Pb^{2+} -doping efficiency in Mn^{2+} -hybrid halide materials, all the powders were characterized by SEM and X-ray photoelectron spectroscopy (XPS) depth profiling data analysis in Figure 3 and Figures S3–S7. The Mn/Pb molar ratios of 1, 4, and 5 show the results corresponding to the input ratios at different etching levels. The Mn/Pb molar ratio of 2 is lower than that

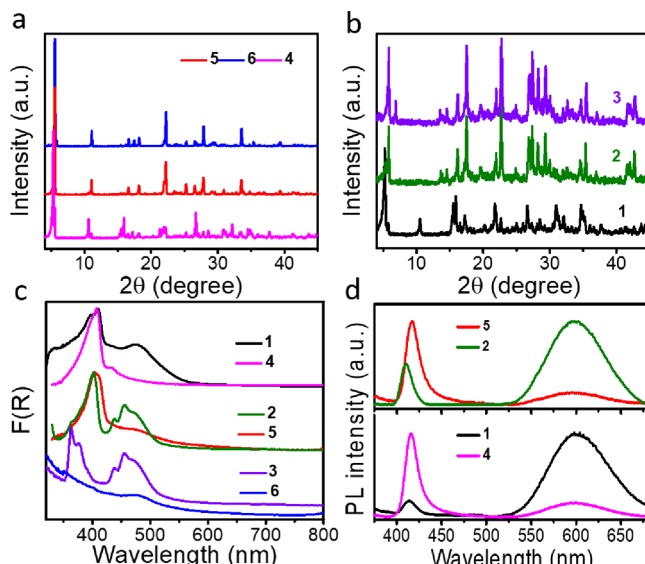


Figure 2. Powder XRD patterns of the (a) 2D structure of 4–6 and (b) 0D structure of 1–3. (c) UV-vis absorption spectra of 1–6. (d) PL spectra of 1, 2, 4, and 5.

properties and XRD pattern (Figure 2, Figures S1 and S2 in the Supporting Information). The (00l) and (113) lattice planes of 4–6 are referred to the simulated 2D $(\text{PEA})_2\text{MnCl}_4$ (#CCDC 258590)³⁶ in Figure S1. The XRD pattern of 6 matches well with 2D $(\text{PEA})_2\text{MnCl}_4$ accompanied by a peak shift to large angles. The interlayer d -spacing is calculated to be 1.6 nm, corresponding to the low-angle diffraction peak at 5.52°.³⁷ The characteristic layer structures of 4 and 5 are identified by matching XRD patterns with 6. The XRD peaks

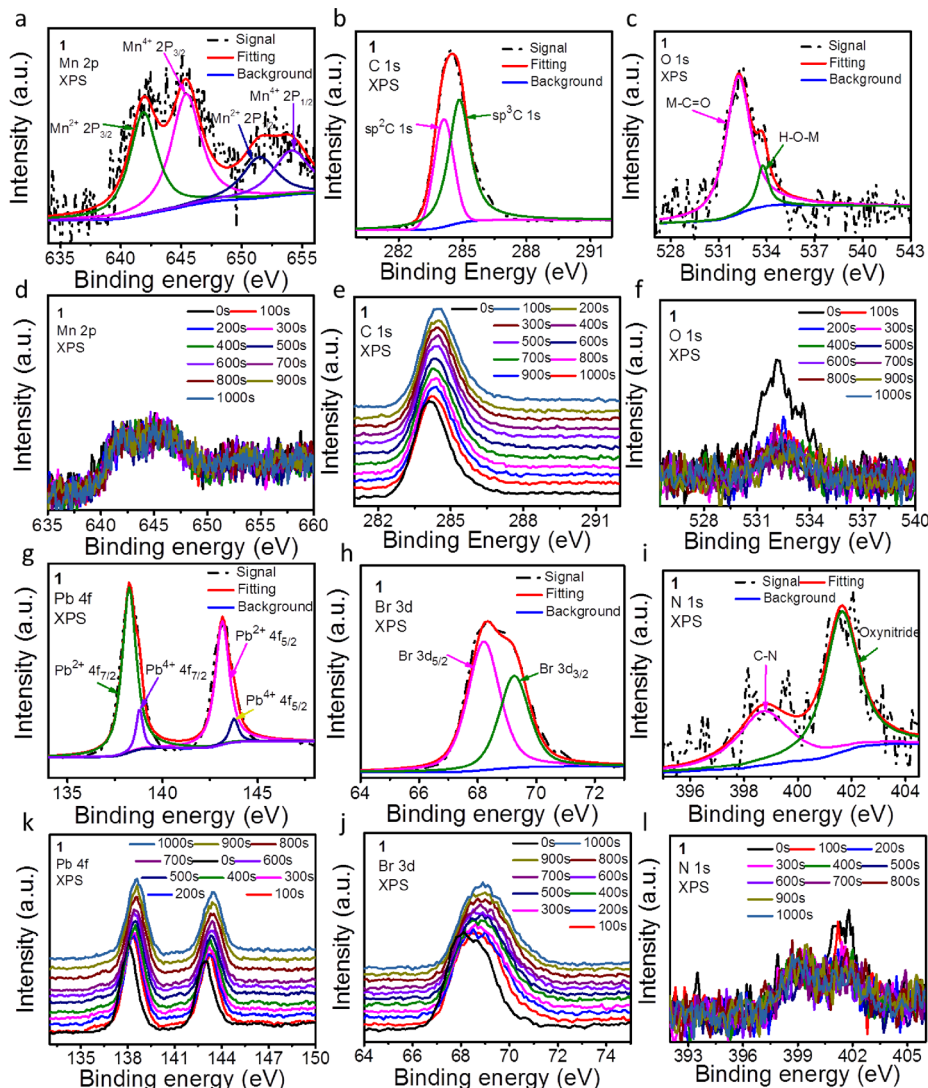


Figure 3. High-resolution deconvoluted XPS spectra for (a) Mn 2p, (b) C 1s, (c) O 1s, (g) Pb 4f, (h) Br 3d, and (i) N 1s collected on perovskite 1. Depth profiling spectra of (d) Mn 2p, (e) C 1s, (f) O 1s, (j) Pb 4f, (k) Br 3d, and (l) N 1s collected on 1.

of the precursors, which can be ascribed to heterogeneous doping. Deviating the Mn/Pb atomic ratio in **5** from the ideal ratio also reveals the heterogeneous doping efficiency. The energy dispersive X-ray diffraction (EDS) and mapping in the selected area of each compound are shown in Figures S8–S15. Table 1 lists the Mn:Pb atomic ratios. The Mn/Pb atomic ratio of a single particle is consistent with the input amount of reactants. We determined that Pb²⁺ is successfully doped in the crystal structure. From high-resolution XPS measurements, we obtain the detailed elemental information (C 1s, N 1s, O 1s, Mn 2p, Pb 4f, Br 3d) of all compounds, and the detailed

analyses are in the Supporting Information. Both Pb²⁺ and Mn²⁺ are present in **1**, **2**, **4**, and **5**. Similar situations are noted in **3** and **6**, except for missing Pb²⁺ in the XPS patterns.

The pure Mn complex **6** has the general formula (PEA)₂MnBr₄. Therefore, we classified **6** as a 2D perovskite while other compounds are Pb-doped complexes. The local coordination number of Mn²⁺ is 6. Thus, the term-symbols of the Mn multiplets are given in terms of the O_h symmetry. We reveal that the composition and dimension of perovskite materials can be easily tuned by the reverse doping method. This is the first time this interesting phenomenon was observed in Mn²⁺-hybrid halide.

After investigating the correlation between water-stable performance and the structure of the layered perovskites (Table S1), we note that the Mn²⁺ concentration and dimension are closely related to the water stability. Mn²⁺-doped 2D Pb²⁺ perovskites were widely reported for their excellent device performance.^{13,48} However, all of them showed stability in only humid conditions as well as low concentration of dopant ions in the final compounds even though a large amount of Mn halide salt was taken in solution. Generally, the Mn²⁺-doping level in the perovskite lattice is

Table 1. Composition Analysis and Optical Properties for Quasi Lead-Free Mn-Based Perovskite (1, 2, 4, 5)

sample	Mn:Pb atomic ratio			PL-QY (%)
	input	EDS	XPS	
1	1	0.8	1.19	67
2	15	16.8	3.44	58
4	1	1.06	1.36	36.9
5	15	17.5	15.88	52.7

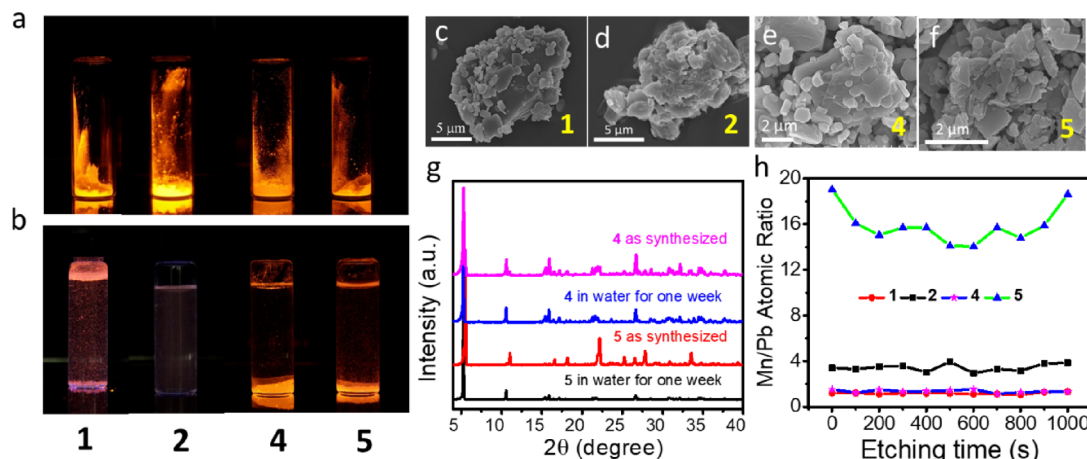


Figure 4. Solid powder images of **1**, **2**, **4**, and **5** under (a) 365 nm UV irradiation and (b) 365 nm UV irradiation after immersion in water. Representative SEM morphology images of (c) **4**, (d) **5**, (e) **4** after immersing in water, and (f) **5** after immersing in water. (g) XRD patterns of **4** and **5** before and after immersing in water. (h) Atomic ratio of Mn to Pb in XPS depth profiling of powders **1**, **2**, **4**, and **5**.

limited because Mn^{2+} and Pb^{2+} have quite different sizes, leading to large strain inside the lattice.⁴⁹ In this work, instead of the commonly adopted doping process where Mn^{2+} is doped in lead halide perovskite, we develop a new strategy to make B-site-doped quasi-lead-free Mn^{2+} perovskites. We present the doping efficiency and corresponding PL-QY values for **1–6** in Table 1. Mn-based perovskites with less Pb^{2+} dopant are successfully synthesized with the largest molar ratio of Mn/Pb as high as 95%.

4 and **5** exhibit good water durability and stability, shown in Figure 4a,b, with slightly decayed luminescence after immersing in water, while compounds **2**, **3**, and **6** decompose quickly. Compounds **4** and **5** are highly stable even after immersing in water, retaining their bright orange luminescence. The stability and morphologies of these samples are verified by XRD and SEM-EDS analyses. The hydrophobic nature of the PEA^+ cation and the structural distortions due to Pb^{2+} doping work in synergy. The PEA^+ cation creates a surface barrier that repels water, while the distorted lattice structure, with its higher formation energy, further resists water infiltration. This cooperative effect makes it challenging for water to penetrate the crystal lattice, ensuring long-term stability in aqueous environments. The structure and morphology of **4** and **5** are confirmed before and after immersing in water, as shown in Figure 4c–g. Powder XRD patterns of **4** and **5** after immersing in water are conducted (Figure 4g). The compounds after immersing in water exhibit similar XRD patterns that match the rich Pb^{2+} perovskite phase **4** from the magnified high-pressure XRD pattern (Figure 4g, Figure S21). Water-sensitive components are decomposed, and a water-stable rich Pb^{2+} perovskite phase is retained. In Figures S8–S13, the EDS results show that the dried powder, after immersing in water, has Mn/Pb atomic ratios of 0.8 for **4**, and 1.4 for **5**. Their morphologies exhibit dense nanosheets, which gives additional evidence for the water-stable perovskite structure. We hypothesize that the water stability of perovskites is correlated with its morphology and doping efficiency for the layered perovskites. Because of the high specific surface area of the formed microcrystals, single sheets are self-assembled into a layered structure with the assistance of PEA^+ . The SEM morphology images of **4** and **5** in Figure 4 give the water-stable perovskite morphology in detail. The powder morphologies before and after immersing in water show similar self-

assembled structures. Thus, we conclude that a proper Mn/Pb atomic ratio enhances the water stability of the layered structure.

Energy transfer-induced orange luminescence is widely discussed in Mn^{2+} -doped Pb^{2+} -based perovskites.^{3,28,48} Excitons in host are transferred to Mn^{2+} emission centers inducing $Mn^{2+}6A_1-4T_1$ emission. In the case of our as-synthesized Pb^{2+} -doped Mn-based perovskites, the energy transfer occurs from Pb^{2+} to Mn^{2+} in the 2D and 0D bulk crystals while it is more efficient in the 0D structure as evidenced from PL QY measurement (Table 1 and Figure S22). The enhanced efficiency of energy transfer from Pb^{2+} to Mn^{2+} in the 0D structure of our as-synthesized Pb^{2+} -doped Mn-based perovskites can be attributed to the unique confinement effects and reduced structural defects in the zero-dimensional system. In the 0D structure, both dopants are confined within a nanoscale volume, promoting a higher probability of interaction and efficient energy transfer. Additionally, the quantization of energy levels in the lower-dimensional structure aligns the electronic states of Pb^{2+} and Mn^{2+} more favorably, facilitating resonant energy transfer. The reduced defects and structural imperfections in the 0D structure further minimize energy losses, making it the preferred configuration for optimizing the energy transfer efficiency between Pb^{2+} and Mn^{2+} ions. Optical properties are characterized by UV-vis and PL spectroscopy in Figure 2c,d. **4** and **5** exhibit dual emission peaks centered at nearly 416 and 597 nm, while their absorption spectra exhibit only one peak centered at 406 nm. This can be dominated by energy transfer between the activator Pb^{2+} and emitter Mn^{2+} coexisting in the 2D microcrystals. A weak tail ranging from 435 to 600 nm is attributed to absorption by the octahedron $[MnBr_4]^{2-}$ inorganic layer (Figure 2).⁴² Similarly, **1** shows absorption peaks of both octahedron $[PbBr_6]^{4-}$ and tetrahedron $[MnBr_4]^{2-}$ moieties, while dual emission spectra are observed with a weak peak centered at 411 nm and a greatly enhanced broad peak centered at 600 nm. For **2**, the same situation appears with the PL peak, which shifts to 409 and 598 nm. The slight discrepancy between 2D and 0D structures is because more Mn^{2+} emitters surround the Pb^{2+} activator in the 0D crystal structure and highly efficient energy transfer occurs. As a result, **1** and **2** exhibit higher PLQY, which reach 67 and 58%, respectively (Table 1). When the 0D phase is converted

to a 2D phase, a reverse emission situation appears and the PL-QY reduces to 36.9 and 52.7%, respectively. We note that excitons under constraints in the lattice restrict the efficient interaction between the activator and emitter. To give a more detailed evidence to the energy transfer process, we perform PL measurements under excited wavelengths at 350, 415, and 460 nm (Figure S16). When excited with a laser beam energy above 450 nm, a distinctive emission peak of Mn^{2+} is observed. However, when excited with a lower-energy laser beam than the band gap of the activator, the intensity of the broad emission peak disappears gradually. The gradual disappearance of the intensity of broad emission peaks when excited with a lower-energy laser beam than the band gap of the activator can be attributed to the mismatch between the excitation energy and the energy required to create electron–hole pairs in the material. When excited with a laser beam above 450 nm (higher energy), there is enough energy to generate a significant number of excited states in the activator ions, resulting in a distinctive emission peak from Mn^{2+} . However, when excited with lower-energy photons, insufficient energy is available to create these excited states efficiently. As a result, fewer electrons are promoted to higher energy levels, reducing the population of excited states available for emission and leading to the gradual disappearance of the emission peak. This phenomenon reflects the importance of matching the excitation energy to the band gap of the activator for efficient luminescence in such materials. Thus, we confirm that the bright-orange luminescence is attributed to the energy transfer from the exciton activated by Pb^{2+} to the emitter Mn^{2+} .⁴⁸ 3 and 6 exhibit no fluorescence under UV light. This is attributed to the Mn–Mn coupling interactions, resulting in nonradiative recombination within pure Mn compounds. However, all of the doped compounds show bright-pink fluorescence. This is attributed to the change in local environment of Mn^{2+} upon doping with Pb^{2+} , and consequently, the charge transfer occurs from the Pb^{2+} activator to the Mn^{2+} emitter exhibiting bright fluorescence. Previously, it was reported that the red emission of Mn complexes stems from $^6\text{A}_{1g}$ – $^4\text{T}_{1g}$ O_h transition and the corresponding lifetime of this emission generally appears in microseconds.^{2,10}

From all of the above observations, we have drawn the following mechanism for the energy transfer between the activator Pb^{2+} and the emitter Mn^{2+} of Pb^{2+} -doped Mn^{2+} -based hybrid halides. The highly sensitized orange emission observed upon band-gap excitation signifies a remarkable interplay within the heterometallic (Mn and Pb) halide material.^{2,34,50,51} It demonstrates a strong exchange coupling, indicating a powerful interaction between the free excitons (electron–hole pairs) and the d electrons associated with Mn^{2+} ions. These Mn^{2+} ions play a critical role by acting as efficient energy acceptors, effectively preventing the loss of energy through nonradiative pathways. The photophysical process, illustrated in Figure S23, begins with the material being excited to free exciton states upon exposure to UV radiation. Subsequently, an ultrafast intersystem crossing (ISC) process and internal conversion take place, culminating in the orange emission of light of ~ 600 nm, specifically involving a transition from the $^4\text{T}_{1g}$ to $^6\text{A}_{1g}$ state. Simultaneously, resident-free excitons directly recombine, emitting light at 416 nm. This intricate interplay is driven by the presence of Mn^{2+} ions, introducing a novel recombination pathway ($^4\text{T}_{1g} \rightarrow ^6\text{A}_{1g}$). Additionally, the lead halide framework functions as an efficient energy antenna, effectively capturing and channeling energy to the Mn^{2+}

luminescent centers. Altogether, these processes lead to a substantial enhancement of the PLQY of heterometallic halide hybrid material.

To better understand the new phenomenon, we investigate the optical properties by multiphoton confocal fluorescent microscopy (Figure 5, Figures S17–S20). We focus on the

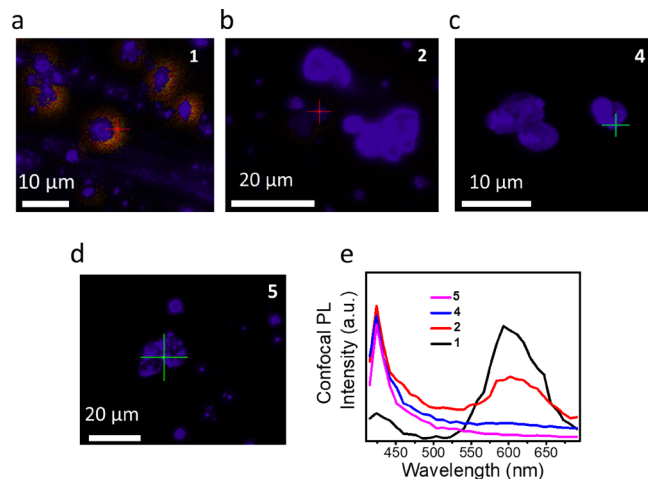


Figure 5. Single-particle photoluminescence images of (a) 1, and (b) 2, (c) 4, (d) 5, and (e) the corresponding single-particle PL emission spectra for microplate-shaped 1, 2, 4, and 5 under laser wavelength 405 nm.

single-particle of each compound to study the fluorescence and PL spectra (Figure 5a–e). 2, 4, and 5 exhibit bright-blue fluorescence with a weak orange color, while 1 shows strong orange fluorescence under 405 nm laser. The bright-orange luminescence of 1, 2, 4, and 5 is obtained under a UV lamp (Figure 4a). Then, the single particle PL spectra in Figure 5e show that each particle exhibits dual emission with similar PL intensity of the powder sample.

CONCLUSIONS

In summary, we have developed for the first time a new strategy to synthesize water-stable Pb^{2+} -doped Mn-based perovskites through a high-energy ball milling method. The structural information and optical properties of the 0D- and 2D-featured Pb^{2+} -doped Mn-based perovskites have been explored in detail. We demonstrate that the key factors contributing to the water stability of 2D Pb^{2+} -doped Mn^{2+} -hybrid halides are a sufficient level of Pb^{2+} doping in the layered structure of the Mn^{2+} -hybrid halide and a high Mn:Pb atomic ratio. Furthermore, for the first time, the energy transfer is observed between the activator Pb^{2+} and the emitter Mn^{2+} of Pb^{2+} -doped Mn^{2+} -based hybrid halides. In traditional synthesis processes, Pb^{2+} cannot be largely substituted because of the lattice strain, so toxicity remains a serious issue that significantly impedes the application of perovskites. This issue has been resolved in this work by a reverse doping process.

ASSOCIATED CONTENT

Supporting Information

The Supporting Information is available free of charge at <https://pubs.acs.org/doi/10.1021/acs.inorgchem.3c02840>.

Full experimental details and analytical data, XPS spectra, SEM-EDS data, confocal microscopy images, and XRD data ([PDF](#))

AUTHOR INFORMATION

Corresponding Author

Tanu Jana — Division of Physics and Semiconductor Science, Dongguk University, Seoul 04620, Republic of Korea;
✉ orcid.org/0000-0001-6566-0438; Email: atanujanaic@gmail.com, atanujana@dongguk.edu

Authors

Qiankai Ba — Center for Superfunctional Materials, Department of Chemistry, Ulsan National Institute of Science and Technology, Ulsan 44919, South Korea; Advanced Solar Technology Institute (ASTI), Xuancheng 242000 Anhui, China; orcid.org/0000-0001-7233-5051

Abhishek Meena — Division of Physics and Semiconductor Science, Dongguk University, Seoul 04620, Republic of Korea

Complete contact information is available at:

<https://pubs.acs.org/10.1021/acs.inorgchem.3c02840>

Author Contributions

The manuscript was written through the contributions of all authors. All authors have given approval to the final version of the manuscript.

Notes

The authors declare no competing financial interest.

ACKNOWLEDGMENTS

This work was supported by the National Research Foundation (NRF) of Korea (grant nos. 2021R1F1A1062528 and 2021R1A4A5031805).

REFERENCES

- (1) Bhargava, R. N.; Gallagher, D.; Hong, X.; Nurmiikko, A. Optical Properties of Manganese-Doped Nanocrystals of ZnS. *Phys. Rev. Lett.* **1994**, *72* (3), 416–419.
- (2) Liu, W.; Lin, Q.; Li, H.; Wu, K.; Robel, I.; Pietryga, J. M.; Klimov, V. I. Mn²⁺-Doped Lead Halide Perovskite Nanocrystals with Dual-Color Emission Controlled by Halide Content. *J. Am. Chem. Soc.* **2016**, *138* (45), 14954–14961.
- (3) Parobek, D.; Roman, B. J.; Dong, Y.; Jin, H.; Lee, E.; Sheldon, M.; Son, D. H. Exciton-to-Dopant Energy Transfer in Mn-Doped Cesium Lead Halide Perovskite Nanocrystals. *Nano Lett.* **2016**, *16* (12), 7376–7380.
- (4) Rodríguez-Lazcano, Y.; Nataf, L.; Rodríguez, F. Electronic Structure and Luminescence of [(CH₃)₄N]₂MnX₄ (X = Cl, Br) Crystals at High Pressures by Time-Resolved Spectroscopy: Pressure Effects on the Mn-Mn Exchange Coupling. *Phys. Rev. B* **2009**, *80* (8), No. 085115.
- (5) Liang, J.; Liu, Z.; Qiu, L.; Hawash, Z.; Meng, L.; Wu, Z.; Jiang, Y.; Ono, L. K.; Qi, Y. Enhancing Optical, Electronic, Crystalline, and Morphological Properties of Cesium Lead Halide by Mn Substitution for High-Stability All-Inorganic Perovskite Solar Cells with Carbon Electrodes. *Adv. Energy Mater.* **2018**, *1800504*, 1–7.
- (6) Zhou, C.; Lin, H.; He, Q.; Xu, L.; Worku, M.; Chaaban, M.; Lee, S.; Shi, X.; Du, M. H.; Ma, B. Low Dimensional Metal Halide Perovskites and Hybrids. *Mater. Sci. Eng. R Rep.* **2019**, *137* (October 2018), 38–65.
- (7) Hu, Y.; Qiu, T.; Bai, F.; Miao, X.; Zhang, S. Enhancing Moisture-Tolerance and Photovoltaic Performances of FAPbI₃ by Bismuth Incorporation. *J. Mater. Chem. A* **2017**, *5* (48), 25258–25265.
- (8) Luo, J.; Im, J.-H.; Mayer, M. T.; Schreier, M.; Nazeeruddin, M. K.; Park, N.-G.; Tilley, S. D.; Fan, H. J.; Gratzel, M. Water Photolysis at 12.3% Efficiency via Perovskite Photovoltaics and Earth-Abundant Catalysts. *Science* **2014**, *345* (6204), 1593–1596.
- (9) Hou, S.; Gangishetty, M. K.; Quan, Q.; Congreve, D. N. Efficient Blue and White Perovskite Light-Emitting Diodes via Manganese Doping. *Joule* **2018**, *2* (11), 2421–2433.
- (10) Zou, S.; Liu, Y.; Li, J.; Liu, C.; Feng, R.; Jiang, F.; Li, Y.; Song, J.; Zeng, H.; Hong, M.; Chen, X. Stabilizing Cesium Lead Halide Perovskite Lattice through Mn(II) Substitution for Air-Stable Light-Emitting Diodes. *J. Am. Chem. Soc.* **2017**, *139* (33), 11443–11450.
- (11) Hao, F.; Stoumpos, C. C.; Cao, D. H.; Chang, R. P. H.; Kanatzidis, M. G. Lead-Free Solid-State Organic-Inorganic Halide Perovskite Solar Cells. *Nat. Photonics* **2014**, *8* (6), 489–494.
- (12) Abdelhady, A. L.; Saidaminov, M. I.; Murali, B.; Adinolfi, V.; Voznyy, O.; Katsiev, K.; Alarousu, E.; Comin, R.; Dursun, I.; Sinatra, L.; Sargent, E. H.; Mohammed, O. F.; Bakr, O. M. Heterovalent Dopant Incorporation for Bandgap and Type Engineering of Perovskite Crystals. *J. Phys. Chem. Lett.* **2016**, *7* (2), 295–301.
- (13) Zhou, Y.; Chen, J.; Bakr, O. M.; Sun, H. T. Metal-Doped Lead Halide Perovskites: Synthesis, Properties, and Optoelectronic Applications. *Chem. Mater.* **2018**, *30* (19), 6589–6613.
- (14) Zhou, D.; Liu, D.; Pan, G.; Chen, X.; Li, D.; Xu, W.; Bai, X.; Song, H. Cerium and Ytterbium Codoped Halide Perovskite Quantum Dots: A Novel and Efficient Downconverter for Improving the Performance of Silicon Solar Cells. *Adv. Mater.* **2017**, *29* (42), 1–6.
- (15) Zhao, S.; Jia, Z.; Huang, Y.; Qian, Q.; Lin, Q.; Zang, Z. Solvent-Free Synthesis of Inorganic Rubidium Copper Halides for Efficient Wireless Light Communication and X-Ray Imaging. *Adv. Funct. Mater.* **2023**, DOI: [10.1002/adfm.202305858](https://doi.org/10.1002/adfm.202305858).
- (16) Ma, W.; Liang, D.; Qian, Q.; Mo, Q.; Zhao, S.; Cai, W.; Chen, J.; Zang, Z. Near-Unity Quantum Yield in Zero-Dimensional Lead-Free Manganese-Based Halides for Flexible X-Ray Imaging with High Spatial Resolution. *eScience* **2023**, *3* (2), No. 100089.
- (17) Mo, Q.; Yu, J.; Chen, C.; Cai, W.; Zhao, S.; Li, H.; Zang, Z. Highly Efficient and Ultra-Broadband Yellow Emission of Lead-Free Antimony Halide toward White Light-Emitting Diodes and Visible Light Communication. *Laser Photon. Rev.* **2022**, *16* (10), 1–8.
- (18) Zhao, S.; Chen, C.; Cai, W.; Li, R.; Li, H.; Jiang, S.; Liu, M.; Zang, Z. Efficiently Luminescent and Stable Lead-free Cs₃Cu₂Cl₅@Silica Nanocrystals for White Light-Emitting Diodes and Communication. *Adv. Opt. Mater.* **2021**, *9* (13), 1–9.
- (19) Jana, A.; Zhumagali, S.; Ba, Q.; Nissimagoudar, A. S.; Kim, K. S. Direct Emission from Quartet Excited States Triggered by Upconversion Phenomena in Solid-Phase Synthesized Fluorescent Lead-Free Organic-Inorganic Hybrid Compounds. *J. Mater. Chem. A* **2019**, *7* (46), 26504–26512.
- (20) Leng, M.; Chen, Z.; Yang, Y.; Li, Z.; Zeng, K.; Li, K.; Niu, G.; He, Y.; Zhou, Q.; Tang, J. Lead-Free, Blue Emitting Bismuth Halide Perovskite Quantum Dots. *Angew. Chemie Int. Ed.* **2016**, *55* (48), 15012–15016.
- (21) Liu, X.; Wu, T.; Luo, X.; Wang, H.; Furue, M.; Bessho, T.; Zhang, Y.; Nakazaki, J.; Segawa, H.; Han, L. Lead-Free Perovskite Solar Cells with Over 10% Efficiency and Size 1 cm² Enabled by Solvent-Crystallization Regulation in a Two-Step Deposition Method. *ACS Energy Lett.* **2022**, *7* (1), 425–431.
- (22) Jana, A.; Sree, V. G.; Ba, Q.; Cho, S. C.; Lee, S. U.; Cho, S.; Jo, Y.; Meena, A.; Kim, H.; Im, H. Efficient Organic Manganese(II) Bromide Green-Light-Emitting Diodes Enabled by Manipulating the Hole and Electron Transport Layer. *J. Mater. Chem. C* **2021**, *9* (34), 11314–11323.
- (23) Zhou, Y.; Zhao, Y. Chemical Stability and Instability of Inorganic Halide Perovskites. *Energy Environ. Sci.* **2019**, *12* (5), 1495–1511.
- (24) Das Adhikari, S.; Dutta, S. K.; Dutta, A.; Guria, A. K.; Pradhan, N. Chemically Tailoring the Dopant Emission in Manganese-Doped CsPbCl₃ Perovskite Nanocrystals. *Angew. Chemie - Int. Ed.* **2017**, *56* (30), 8746–8750.

- (25) Liu, H.; Wu, Z.; Shao, J.; Yao, D.; Gao, H.; Liu, Y.; Yu, W.; Zhang, H.; Yang, B. $\text{CsPb}_x\text{Mn}_{1-x}\text{Cl}_3$ Perovskite Quantum Dots with High Mn Substitution Ratio. *ACS Nano* **2017**, *11* (2), 2239–2247.
- (26) Huang, G.; Wang, C.; Xu, S.; Zong, S.; Lu, J.; Wang, Z.; Lu, C.; Cui, Y. postsynthetic Doping of MnCl_2 Molecules into Preformed CsPbBr_3 Perovskite Nanocrystals via a Halide Exchange-Driven Cation Exchange. *Adv. Mater.* **2017**, *29* (29), 1–5.
- (27) Dutta, S. K.; Dutta, A.; Das Adhikari, S.; Pradhan, N. Doping Mn^{2+} in Single-Crystalline Layered Perovskite microcrystals. *ACS Energy Lett.* **2019**, *4* (1), 343–351.
- (28) Biswas, A.; Bakthavatsalam, R.; Kundu, J. Efficient Exciton to Dopant Energy Transfer in Mn^{2+} -Doped $(\text{C}_4\text{H}_9\text{NH}_3)_2\text{PbBr}_4$ Two-Dimensional (2D) Layered Perovskites. *Chem. Mater.* **2017**, *29* (18), 7816–7825.
- (29) Ba, Q.; Jana, A.; Wang, L.; Kim, K. S. Dual Emission of Water-Stable 2D Organic–Inorganic Halide Perovskites with Mn(II) Dopant. *Adv. Funct. Mater.* **2019**, *1904768* (I), 1904768.
- (30) Eperon, G. E.; Ginger, D. S. B-Site Metal Cation Exchange in Halide Perovskites. *ACS Energy Lett.* **2017**, *2* (5), 1190–1196.
- (31) Sun, C.; Gao, Z.; Deng, Y.; Liu, H.; Wang, L.; Su, S.; Li, P.; Li, H.; Zhang, Z.; Bi, W. Emission Tunable Mn Doped Two-Dimensional Perovskites with High Luminescence and Stability. *ACS Appl. Mater. Interfaces* **2019**, 34109.
- (32) Liu, Y.; Zhang, J.; Han, B.; Wang, X.; Wang, Z.; Xue, C.; Bian, G.; Hu, D.; Zhou, R.; Li, D. S.; Wang, Z.; Ouyang, Z.; Li, M.; Wu, T. New Insights into Mn-Mn Coupling Interaction-Directed Photoluminescence Quenching Mechanism in Mn^{2+} -Doped Semiconductors. *J. Am. Chem. Soc.* **2020**, *142* (14), 6649–6660.
- (33) Pan, G.; Bai, X.; Yang, D.; Chen, X.; Jing, P.; Qu, S.; Zhang, L.; Zhou, D.; Zhu, J.; Xu, W.; Dong, B.; Song, H. Doping Lanthanide into Perovskite Nanocrystals: Highly Improved and Expanded Optical Properties. *Nano Lett.* **2017**, *17* (12), 8005–8011.
- (34) Zhang, H.; Yao, J.; Yang, Y.; Fu, H. Tailoring Color-Tunable Dual Emissions of Mn^{2+} -Alloyed Two-Dimensional Perovskite Quantum Wells. *Chem. Mater.* **2021**, *33* (8), 2847–2854.
- (35) Ji, S.; Yuan, X.; Liu, Z.; Zhao, L.; Zhao, K.; Zheng, J.; Zhao, J.; Wang, J. Photo- and Thermal-Induced Ion Migration and Phase Separation in Mn-Doped Two-Dimensional PEA_2PbX_4 Perovskite. *ACS Appl. Mater. Interfaces* **2023**, *15* (27), 33087–33094.
- (36) Park, S. H.; Oh, I. H.; Park, S.; Park, Y.; Kim, J. H.; Huh, Y. D. Canted Antiferromagnetism and Spin Reorientation Transition in Layered Inorganic–Organic Perovskite $(\text{C}_6\text{H}_5\text{CH}_2\text{CH}_2\text{NH}_3)_2\text{MnCl}_4$. *Dalt. Trans.* **2012**, *41* (4), 1237–1242.
- (37) Park, G.; Oh, I. H.; Park, J. M. S.; Jung, J.; You, C. Y.; Kim, J. S.; Kim, Y.; Jung, J. H.; Hur, N.; Kim, Y.; Kim, J. Y.; Hong, C. S.; Kim, K. Y. Solvent-Dependent Self-Assembly of Two Dimensional Layered Perovskite $(\text{C}_6\text{H}_5\text{CH}_2\text{CH}_2\text{NH}_3)_2\text{MCl}_4$ ($\text{M} = \text{Cu}, \text{Mn}$) Thin Films in Ambient Humidity. *Sci. Rep.* **2018**, *8* (1), 1–10.
- (38) Arend, H.; Tichy, K.; Baberschke, K.; Rys, F. Chloride Perovskite Layer Compounds Of. *Solid State Commun.* **1976**, *18*, 999–1003.
- (39) Gao, W.; Leng, M.; Hu, Z.; Li, J.; Li, D.; Liu, H.; Gao, L.; Niu, G.; Tang, J. Reversible Luminescent Humidity Chromism of Organic–Inorganic Hybrid $\text{PEA}_2\text{MnBr}_4$ Single Crystals. *Dalt. Trans.* **2020**, *49* (17), 5662–5668.
- (40) Xu, L. J.; Sun, C. Z.; Xiao, H.; Wu, Y.; Chen, Z. N. Green-Light-Emitting Diodes Based on Tetrabromide Manganese(II) Complex through Solution Process. *Adv. Mater.* **2017**, *29* (10), 2–6.
- (41) Kawano, N.; Koshimizu, M.; Sun, Y.; Yahaba, N.; Fujimoto, Y.; Yanagida, T.; Asai, K. Effects of Organic Moieties on Luminescence Properties of Organic-Inorganic Layered Perovskite-Type Compounds. *J. Phys. Chem. C* **2014**, *118* (17), 9101–9106.
- (42) Li, M.; Zhou, J.; Zhou, G.; Molokeev, M. S.; Zhao, J.; Morad, V.; Kovalenko, M. V.; Xia, Z. Hybrid Metal Halides with Multiple Photoluminescence Centers. *Angew. Chemie - Int. Ed.* **2019**, *58* (51), 18670–18675.
- (43) Guria, A. K.; Dutta, S. K.; Adhikari, S. D.; Pradhan, N. Doping Mn^{2+} in Lead Halide Perovskite Nanocrystals: Successes and Challenges. *ACS Energy Lett.* **2017**, *2* (5), 1014–1021.
- (44) Dutta, A.; Behera, R. K.; Deb, S.; Baitalik, S.; Pradhan, N. Doping Mn(II) in All-Inorganic Ruddlesden–Popper Phase of Tetragonal $\text{Cs}_2\text{PbCl}_3\text{I}_2$ Perovskite Nanoplatelets. *J. Phys. Chem. Lett.* **2019**, *10* (8), 1954–1959.
- (45) Mir, W. J.; Jagadeeswararao, M.; Das, S.; Nag, A. Colloidal Mn-Doped Cesium Lead Halide Perovskite Nanoplatelets. *ACS Energy Lett.* **2017**, *2* (3), 537–543.
- (46) Morad, V.; Cherniukh, I.; Pötschacher, L.; Shynkarenko, Y.; Yakunin, S.; Kovalenko, M. V. Manganese(II) in Tetrahedral Halide Environment: Factors Governing Bright Green Luminescence. *Chem. Mater.* **2019**, *31* (24), 10161–10169.
- (47) Arunkumar, P.; Gil, K. H.; Won, S.; Unithrattil, S.; Kim, Y. H.; Kim, H. J.; Im, W. B. Colloidal Organolead Halide Perovskite with a High Mn Solubility Limit: A Step Toward Pb-Free Luminescent Quantum Dots. *J. Phys. Chem. Lett.* **2017**, *8* (17), 4161–4166.
- (48) Smith, M. D.; Connor, B. A.; Karunadasa, H. I. Tuning the Luminescence of Layered Halide Perovskites. *Chem. Rev.* **2019**, *119* (5), 3104–3139.
- (49) Li, Z. J.; Hofman, E.; Davis, A. H.; Khammang, A.; Wright, J. T.; Dzikovski, B.; Meulenberg, R. W.; Zheng, W. Complete Dopant Substitution by Spinodal Decomposition in Mn-Doped Two-Dimensional CsPbCl_3 Nanoplatelets. *Chem. Mater.* **2018**, *30* (18), 6400–6409.
- (50) Peng, Y.; Li, L.; Ji, C.; Wu, Z.; Wang, S.; Liu, X.; Yao, Y.; Luo, J. Tailored Synthesis of an Unprecedented Pb–Mn Heterometallic Halide Hybrid with Enhanced Emission. *J. Am. Chem. Soc.* **2019**, *141* (31), 12197–12201.
- (51) Paul, S.; Bladt, E.; Richter, A. F.; Döblinger, M.; Tong, Y.; Huang, H.; Dey, A.; Bals, S.; Debnath, T.; Polavarapu, L.; Feldmann, J. Manganese-Doping-Induced Quantum Confinement within Host Perovskite Nanocrystals through Ruddlesden–Popper Defects. *Angew. Chemie Int. Ed.* **2020**, *59* (17), 6794–6799.